Measuring pulse times of arrival from broad-band pulsar observations

K Liu, G. Desvignes, Ismaël Cognard, B.W. Stappers, J.P W. Verbiest, K.J. Lee, D.J. Champion, M Kramer, P.C.C. Freire, R Karuppusamy

Measuring pulse times of arrival from broad-band pulsar observations

K. Liu,[1,2]⋆ G. Desvignes,[3] I. Cognard,[1,2] B. W. Stappers,[4] J. P. W. Verbiest,[3,5] K. J. Lee,[3,6] D. J. Champion,[3] M. Kramer,[3,4] P. C. C. Freire[3] and R. Karuppusamy[3]

[1]*Station de Radioastronomie de Nançay, Observatoire de Paris, CNRS/INSU, F-18330 Nançay, France*
[2]*Laboratoire de Physique et Chimie de l'Environnement et de l'Espace LPC2E CNRS-Université d'Orléans, F-45071 Orléans Cedex 02, France*
[3]*Max-Planck-Institut für Radioastronomie, Auf dem Hügel 69, D-53121 Bonn, Germany*
[4]*University of Manchester, Jodrell Bank Centre of Astrophysics, Alan-Turing Building, Manchester M13 9PL, UK*
[5]*Fakultät für Physik, Universität Bielefeld, Postfach 100131, D-33501 Bielefeld, Germany*
[6]*KIAA, Peking University, Beijing 100871, P.R. China*

ABSTRACT

In recent years, instrumentation enabling pulsar observations with unprecedentedly high fractional bandwidth has been under development which can be used to substantially improve the precision of pulsar timing experiments. The traditional template-matching method used to calculate pulse times of arrival (ToAs) may not function effectively on these broad-band data due to a variety of effects such as diffractive scintillation in the interstellar medium, profile variation as a function of frequency, dispersion measure (DM) evolution, and so forth. In this paper, we describe the channelized discrete Fourier transform method that can greatly mitigate the influence of the aforementioned effects when measuring ToAs from broad-band timing data. The method is tested on simulated data, and its potential in improving timing precision is shown. We further apply the method to PSR J1909−3744 data collected at the Nançay Radio Telescope with the Nançay Ultimate Pulsar Processing Instrument. We demonstrate removal of systematics due to the scintillation effect as well as improvement on ToA measurement uncertainties. Our method also determines temporal variations in DM, which are consistent with multichannel timing approaches used earlier.

Key words: methods: data analysis – pulsars: general – pulsars: individual (PSR J1909−3744).

1 INTRODUCTION

High-precision pulsar timing is the essential tool in the currently ongoing gravity tests with binary pulsars (e.g. Freire et al. 2012; Antoniadis et al. 2013) and gravitational wave detection with pulsar timing arrays (e.g. Hellings & Downs 1983; Foster & Backer 1990). Developments in observing backends based on polyphase filter bank techniques now allow pulsar observations with large fractional bandwidth (e.g. ≳1/3; see Ransom et al. 2009; Stappers et al. 2011; Cognard et al. 2013). Broad-band systems such as the ultra-broad-band (UBB) receiver developed at the Effelsberg radio telescope which achieves an instantaneous frequency coverage from 600 MHz to 3 GHz are being implemented (Karuppusamy et al., in preparation). Extending the observing bandwidth greatly increases the signal-to-noise ratio (S/N) of the observed pulsar profiles which can be translated into a decrease in measurement uncertainties of pulse times of arrival (ToAs; Downs & Reichley 1983). This is likely to improve the resulting pulsar timing precision, under the

circumstance that the actual timing residuals are dominated by white noise (Cordes & Shannon 2010; Liu et al. 2011).

Typically, determination of ToAs is achieved by first correcting for any frequency-dependent delays caused by dispersion in the interstellar medium, then averaging the data across all frequency channels and finally cross-correlating the resulting pulse profile with a template (Taylor 1992). The template can either be a high-S/N profile obtained directly from observations or an analytic model of the pulse (e.g. Kramer et al. 1999). However, applying this approach to broad-band pulsar timing data may be problematic for a number of reasons as follows.

(i) The pulse profile shape is not constant across the observing bandwidth. This can be due to intrinsic profile variation across frequency, frequency-dependent scattering time-scales, instrumental channelization, and so forth. When the observed flux density at different frequencies varies in time due to interstellar scintillation, the shape of the frequency-averaged profile will be changed depending on which part of the band scintillates up and which part scintillates down. In turn, this variation in profile shape will affect the cross-correlation and therefore the derived ToAs (e.g. Liu et al. 2011).

⋆ E-mail: kliu.psr@googlemail.com

(ii) In many cases, the pulsar dispersion measure[1] (DM) has been witnessed to evolve in time (e.g. Keith et al. 2013). Hence, applying a constant but not perfectly correct DM value for dedispersion would smear the profile shape differently as the DM values vary, and thus shift the ToAs. Using an incorrect DM can also induce misalignment of profiles from different frequencies, which would mimic profile variation across the observing band and enhance the scintillation effect mentioned above.

(iii) Variations in the radio frequency interference (RFI) environment can change the usable frequency channels in different observations. This effectively changes the frequency range from which the frequency-averaged profile is composed of due to the frequency dependence of the pulse profile shape. Similar variations in the frequencies used (and therefore in the resulting profile shape) could be caused by instrumental failure or slight changes to the observing system.

Consequently, an alternative approach that utilizes the data's frequency information to avoid the corrupting effects listed above is required. Without frequency averaging, any frequency-dependent changes in brightness will no longer result in changes in the overall pulse shape. DM variations can also be taken into account effectively if the data cover a large enough frequency range.

Besides the current standard template-matching scheme in Taylor (1992), there are also alternative methods targeting different issues. Hotan, Bailes & Ord (2005) applied Gaussian interpolation when cross-correlating profiles with low S/Ns. van Straten (2006) used full Stokes information rather than only the total intensity for ToA determination. Osłowski et al. (2011) decomposed profiles in principal components to improve ToA measurements when the timing residuals are dominated by pulse phase jitter. In this paper, we develop a method to measure ToAs based on timing data with frequency information.

The structure of this paper is as follows. In Section 2, we describe our method to generate ToAs with frequency-resolved data. In Section 3, we present results from tests based on simulated data. Application of the method to real data is shown in Section 4. We conclude with a brief discussion in Section 5.

2 METHODOLOGY

In the traditional approach, the observed pulse profile $P(t)$ is described by a one-dimensional array modelled by

$$P(t) = a + bS(t - \Delta\tau) + n(t), \qquad (1)$$

where $S(t)$ is the standard template obtained from previous observations, a is the baseline difference, b is a scaling factor, $\Delta\tau$ is the phase difference between the profile and the template, and $n(t)$ is a noise component. The actual fitting routine is often carried out in the Fourier domain, where after a discrete Fourier transform (DFT), the model can be written as (Taylor 1992)

$$P_k e^{i\theta_k} = aN\delta_k + bS_k e^{i(\phi_k + k\Delta\tau)} + G_k, \quad k = 0, \ldots, N-1, \qquad (2)$$

where P_k and S_k are the amplitudes of the complex Fourier coefficients, θ_k and ϕ_k are the phases, $\delta_k = 1$ ($k = 0$) or 0 ($k \neq 0$), N is the number of frequency bins, and G_k represents random noise equal to the Fourier transform of the sampled noise in the time-domain

profile, $n(t)$. The best estimated value of $\Delta\tau$ can then be found by minimizing the goodness-of-fit statistic

$$\chi^2(b, \tau) = \sum_{k=1}^{N-1} \left| \frac{P_k - bS_k e^{i(\phi_k - \theta_k + k\Delta\tau)}}{\sigma_k} \right|^2, \qquad (3)$$

where σ_k is the root-mean-square intensity of the noise at frequency k.

If the frequency resolution is kept, the data arrays have to be expanded into a second dimension and in this case the dispersive delay of different frequency bands also needs to be taken into account. Mostly, the delay is found to fulfil the scaling of $t_d \propto \mathrm{DM}/f^2$, where f is the observing frequency (Lorimer & Kramer 2005)[2]. Accordingly, one can express the two-dimensional model as

$$P(f, t) = a(f) + b(f)S(f, t - \Delta\tau - \mathcal{D} \times \Delta\mathrm{DM}/f^2)$$
$$+ n(f, t), \qquad (4)$$

where $\mathcal{D}$ is the dispersion constant and $\Delta\mathrm{DM}$ is the difference in dispersion measure between the profile and the template.[3] Note that $\mathcal{D} \times \Delta\mathrm{DM}/f^2$ vanishes when $f \to \infty$. Hence, $\Delta\tau$ can be directly related to the ToA at infinite frequency, which is obtained after correcting the dispersion delay.

Similar to the treatment in the one-dimensional case, one can carry out a DFT individually on each frequency band, and perform a two-dimensional fit over the entire bandwidth for $\Delta\tau$ and $\Delta\mathrm{DM}$. The approach will be later referred to as the 'channelized DFT method'. After the transformations, the model in the frequency domain can be written as

$$P_{j,k} e^{i\theta_{j,k}} = a_j N\delta_k + b_j S_{j,k} e^{i(\phi_{j,k} + k\tau_j)} + G_{j,k}, \qquad (5)$$

where $k = 0, \ldots, N-1$ and $j = 1, \ldots, N_b$; N is the number of bins, N_b is the number of frequency bands, and

$$\tau_j = \frac{\mathcal{D} \times \Delta DM}{f_j^2} \frac{2\pi}{P} + \Delta\tau. \qquad (6)$$

Here τ_j is in units of radians and P is the pulsar's rotational period. The data of different frequencies are assumed to be from a single observation, which means they are aligned in time by default and thus $\Delta\tau$ is constant over the entire band. Following Taylor (1992), a_j is immediately obtained from

$$a_j = \frac{P_{j,0} - b_j S_{j,0}}{N}. \qquad (7)$$

The best estimates of $\Delta\tau$ and $\Delta\mathrm{DM}$ can then be obtained by minimizing the function

$$\chi^2(b_i, \Delta\tau, \Delta\mathrm{DM}) = \sum_{j=1}^{N_b} \sum_{k=1}^{N-1} \left| \frac{P_{j,k} - b_j S_{j,k} e^{i(\phi_{j,k} - \theta_{j,k} + k\tau_j)}}{\sigma_{j,k}} \right|^2. \qquad (8)$$

Here, the same as in Taylor (1992), the likelihood estimator is calculated using all informative frequency harmonics[4]. In order to

[1] DM is defined as the integrated electron density between the Earth and the pulsar.

[2] Further propagation effects in the interstellar medium (e.g. scattering, as shown in Bhat et al. 2004) could introduce other scalings, too, albeit at a less significant level. A quantitative summary of such effects is not within the scope of this paper, but can be found in e.g. Lorimer & Kramer (2005).
[3] In this paper, we use the definition of $\mathcal{D} \equiv 1/K$, where $K \equiv 2.410 \times 10^{-4}$ MHz^{-2} cm^3 pc s^{-1}.
[4] In Taylor (1992), the calculation of χ^2 includes frequency bins only to $N/2$ because the rest are simply a symmetric duplication and would not add any useful information. Decreasing the number of harmonics used for the fitting may risk discarding useful information and thus affecting measurement precision, especially when profiles are narrow or have sharp features so that the high-frequency bins contain significant power.
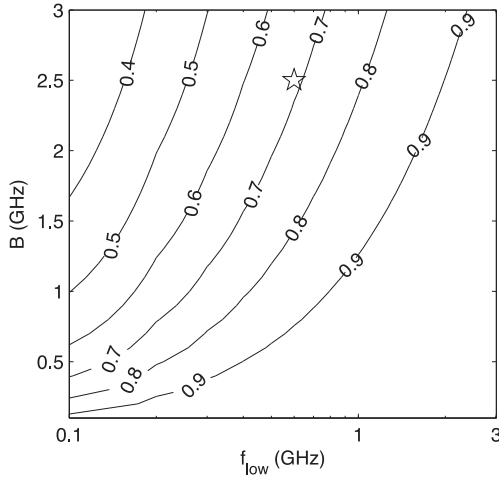
Figure 1. Correlation coefficient (ρ) between $\Delta\tau$ and ΔDM for different bandwidths and frequency ranges. Here f_{low} is the frequency at the lower edge of the bandwidth and ν is the total bandwidth. The Effelsberg UBB setting is represented by the star.

perform the fitting, we modified the Levenberg–Marquardt (L–M) routine in Press et al. (1992) to adopt a model of complex numbers, and recalculated the curvature matrix in this case. More details can be found in Appendix A. The 1σ errors of the fitted parameters are determined from the covariance matrix which is obtained by taking the inverse of the curvature matrix. A similar approach based on the same likelihood estimator as in equation (8), using however a different fitting routine, has been developed by Pennucci, Demorest & Ransom (2014).

It can be seen from the expression of χ^2 in equation (8) that for data with a bandwidth that does not result in a significant difference between f_1 and f_{N_b}, $\Delta\tau$ and ΔDM would be highly correlated. Following the calculation in Lee et al. (2014), in Fig. 1 we plot the correlation coefficient (ρ) between the two parameters for a given observing bandwidth and lower bound of observing frequency. Clearly, $\rho > 0.9$ for all current *L*-band (1–2 GHz) timing observations (with bandwidth <1 GHz), meaning that solely with those data one cannot significantly break the degeneracy between these two parameters. In this case, fitting for both parameters would greatly worsen the accuracy of the obtained value. The UBB receiver on the Effelsberg 100 m radio telescope can significantly decrease the level of correlation, resulting in ρ less than 0.7. Nevertheless, when the observing bandwidth is not enough to be sensitive to a ΔDM fit, one can always choose to fit solely for $\Delta\tau$. Under this circumstance, the likelihood estimator is simplified into

$$\chi^2(b_i, \Delta\tau) = \sum_{j=1}^{N_b} \sum_{k=1}^{N-1} \left| \frac{P_{j,k} - b_j S_{j,k} e^{i(\phi_{j,k} - \theta_{j,k} + k\Delta\tau)}}{\sigma_{j,k}} \right|^2. \quad (9)$$

3 SIMULATIONS

In this section, the channelized DFT method is tested based on simulated data. Here we carried out two types of tests: one to assess the functionality of the algorithm in general and the other to evaluate the potential improvement to ToA measurements when applied in a realistic scenario.

3.1 Test of algorithm functionality

Ideally, a functioning template-matching approach is able to measure the offsets in phase and DM between the profile and the template, as well as their 1σ uncertainties. In the following tests, we simulate data with a bandwidth of 500 MHz, between 1.2 and 1.7 GHz. A Gaussian shape with no frequency dependence is assumed for the two-dimensional template. Individual observations are simulated by adding white noise to the standard profile, until a given S/N is reached. We hereby define the S/N as the ratio of the peak amplitude of the pulse to the rms in the off-pulse region, and use this definition throughout this paper.

3.1.1 Consistency of parameter recovery and uncertainty

In order to show that the method measures the parameters consistently with the calculated errors, we simulated 2×10^4 profiles with randomly distributed offsets in phase and DM with respect to the two-dimensional template. Fig. 2 shows histograms of measured $\Delta\tau$ (top) and ΔDM (bottom) values from the channelized DFT method, after subtraction of the input offsets ($\Delta\tau_i$ and ΔDM$_i$,
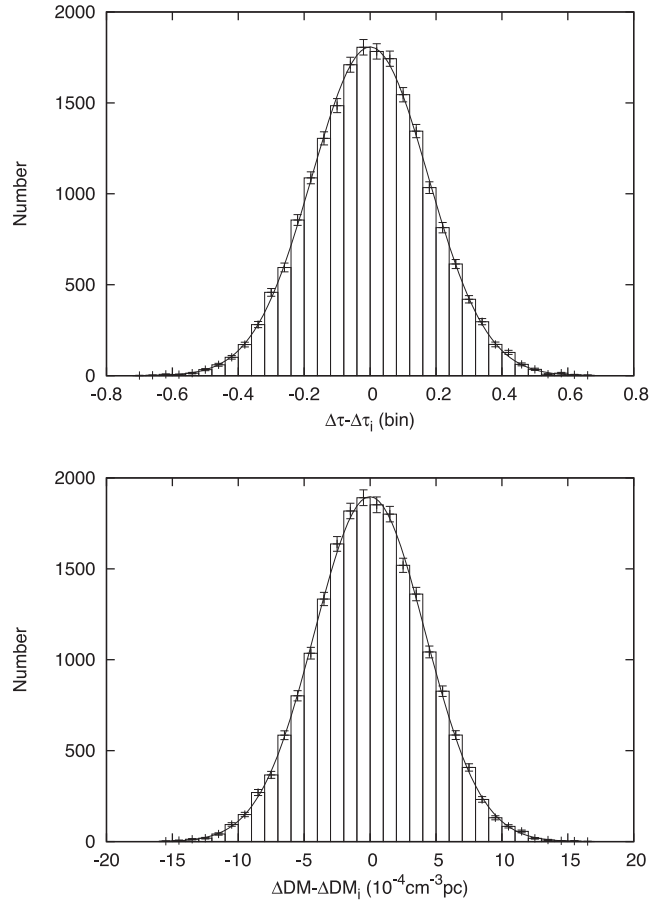

Figure 2. Histograms of measured $\Delta\tau$ (top) and ΔDM (bottom) from 2×10^4 profiles after subtraction of the input values ($\Delta\tau_i$ and ΔDM$_i$, separately). The profiles were simulated with S/N = 100, 16 frequency channels, and randomly distributed $\Delta\tau$ and ΔDM with respect to the template. The distributions are well described by Gaussian functions, with reduced χ^2 of fit close to unity (top: 0.96; bottom: 0.92). The rms in the two cases are 0.176 bins and 4.20×10^{-4} cm^{-3} pc, respectively, consistent with the measurement uncertainties which are 0.177 bins and 4.22×10^{-4} cm^{-3} pc, respectively.

separately). In both cases, the distribution is well described by a Gaussian function and the rms is consistent with expected from the measurement uncertainty.

3.1.2 Consistency of measurement with theoretical expectation

The intrinsic uncertainty of a ToA is expected to be only related to the S/N and the profile shape, and to scale inversely with the S/N (Downs & Reichley 1983). In order to show that the method measures the phase offset with the expected uncertainty, we simulated profiles with different S/Ns and with different numbers of frequency channels. Fig. 3 shows the measured phase uncertainties $\sigma_{\Delta\tau}$ obtained from these profiles. The values were compared with expected measurement uncertainties calculated from the radiometer equation as in Downs & Reichley (1983). Clearly, the uncertainties for data of identical S/N all fully agree with the expectation, and the number of channels has no effect (as is to be expected for a pulse profile with no frequency evolution). Note that for this test the fit of ΔDM has been switched off, as the strong correlation (corresponding to $\rho = 0.982$ in Fig. 1) between ΔDM and $\Delta\tau$ would greatly worsen the measurement uncertainty. In this case, it is not expected that the resulting ToA uncertainties would be the same as calculated from the radiometer equation. Fig. 4 shows the scaling of $\sigma_{\Delta\tau}$ with S/N, as well as the influence of simultaneous ΔDM determination. It can be seen that the scaling follows an inverse trend in either case, with or without simultaneous ΔDM fitting. When both ΔDM and $\Delta\tau$ are fitted, due to the high degree of correlation between these two parameters the measured uncertainties increase substantially (here by a factor of 6).

3.1.3 Reliability of measurement uncertainty in the low-S/N regime

It is known that in the low-S/N regime (e.g. S/N close to unity), the traditional template-matching technique may fail to recover the true phase offset within the measured uncertainty (e.g. Liu 2012). Fig. 5 demonstrates that this is also true for the channelized DFT method. For this test, we generated pulse profiles with the number of frequency channels, N_{chan}, equal to 8, 16, and 32, respectively, and varied the S/N per frequency channel, S/N$_i$, between 1 and 4. For

Figure 4. $\sigma_{\Delta\tau}$ obtained from the channelized DFT method for profiles with different S/Ns. Both cases are presented where ΔDM is simultaneously fitted or not.

Figure 5. Confidence level of $\sigma_{\Delta\tau}$ by the channelized DFT method in the low-S/N regime, based on profiles of different numbers of frequency channels (N_{chan}) and S/N values in individual channels (S/N$_i$). The result achieved with the traditional method (1D) is also shown for comparison.

each combination of N_{chan} and S/N$_i$, we simulated 10^3 profiles and determined how many of these resulted in measurements consistent with the input value for the phase offset (defined by falling into the range decided by the measurement uncertainty), while fitting for $\Delta\tau$ and ΔDM simultaneously. This fraction is shown on the y-axis of Fig. 5. Since the uncertainties are 1σ values, one would expect all points in this plot to fall around a value of 0.68. This is clearly not the case for S/N$_i$ values less than 2.0, and the deviations from 0.68 occur at the same S/N$_i$ value for different channel numbers. The same situation was seen when investigating the consistency of the measured ΔDM values. Statistics of $\Delta\tau$ measurements based on the traditional technique show deviation from 1σ at the same S/N$_i$ value. Therefore, for more reliable measurements in this case, either frequency channels need to be combined to increase the S/N$_i$ or an alternative approach has to be considered (as in e.g. Hotan et al. 2005).

3.1.4 Impact of template with finite S/N

As shown in Liu et al. (2011), using a template which is not entirely noise free may also limit the functionality of the template-matching technique. This issue is demonstrated in Fig. 6, where we evaluated
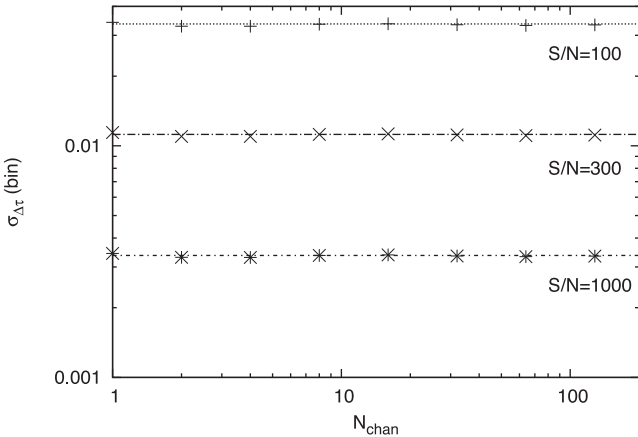

Figure 3. $\sigma_{\Delta\tau}$ obtained from the channelized DFT method for profiles of different S/N values and numbers of channels. The lines represent the expected values from the radiometer equation for different S/Ns. The fractional differences between the precisions and the expectations are all within 2.5 per cent.
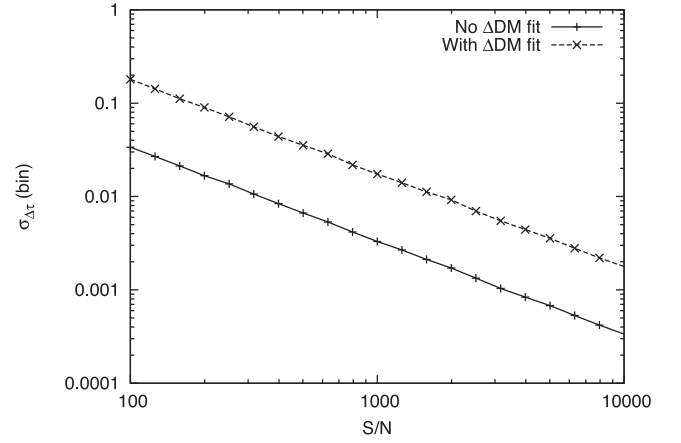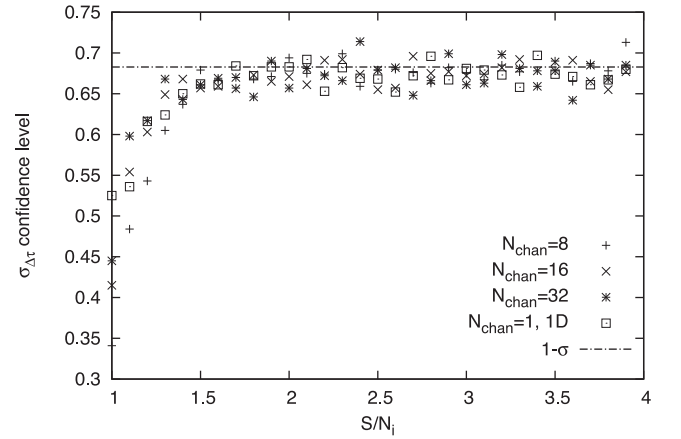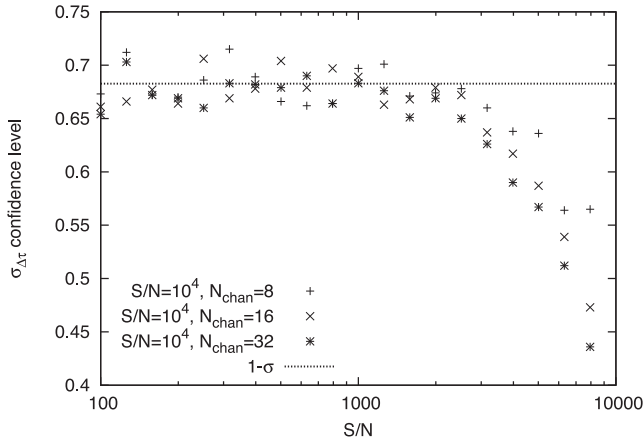
Figure 6. Confidence level of $\sigma_{\Delta\tau}$ from the channelized DFT method, based on templates with S/N $=10^4$ and different numbers of channels.

the accuracy of the measured uncertainties using the same approach as the one followed for Fig. 5, but this time with standard templates of S/N $= 10^4$ and different N_{chan} values. It can be seen that the $\sigma_{\Delta\tau}$ values prove to be reliable, but only until the simulated profiles reach an S/N that is within an order of magnitude of the S/N of the template profile. Therefore, the algorithm works as expected when the template profile has a sufficiently high S/N and the observations have a significantly lower S/N. Also in this case, the impact of the number of frequency channels is limited, though fewer frequency channels (i.e. with higher S/N$_i$ values) do make for slightly more reliable measurement uncertainties. Again, the ΔDM measurements were seen to be influenced by the noise of the template in the same manner.

3.2 Expected improvement on real data

As discussed in Section 1, applying the traditional template-matching approach to broad-band pulsar timing data would not properly produce ToAs in some circumstances. Below, we demonstrate improvements that are achieved using the channelized DFT method. Here, we simulate profiles and conduct the fitting based on a frequency-dependent template model, and examples can be found shown in Fig. 7.

3.2.1 Accounting for DM variations

When the DM of a pulsar varies between observations, using a constant DM value for dedispersion will introduce a bias in the measured ToAs. As discussed in Section 2, when the observing bandwidth is sufficiently large, use of a two-dimensional template can take the influence of variable DMs into consideration when calculating the ToAs. For demonstration purposes, we simulated 100 profiles with Gaussianly distributed DM variations[5] with a standard deviation of 2×10^{-4} cm^{-3} pc. The simulated data have a bandwidth of 500 MHz between 1.2 and 1.7 GHz. The offsets in phase were measured using the channelized DFT method, both with and without a simultaneous fit for ΔDM. From the results in Fig. 8 (top plot, left-hand panel), it is clear that the obtained $\Delta\tau$ values

---

[5] Note that the observed DMs are more likely to show gradual variations (e.g. Keith et al. 2013). Nevertheless, our simulation is enough to demonstrate the improvement by performing a simultaneous fit for $\Delta\tau$ and ΔDM.
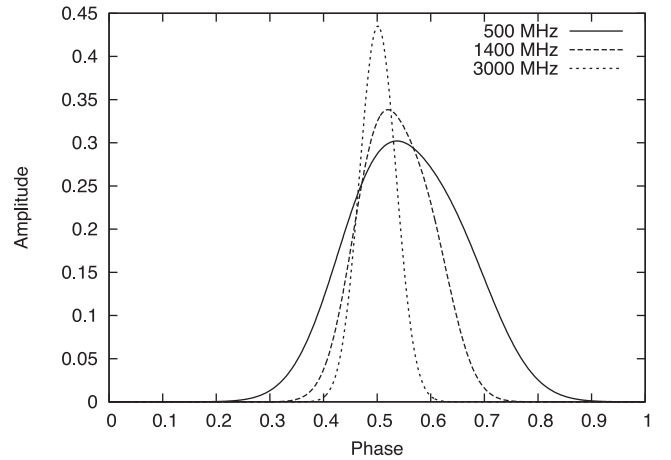
Figure 7. Examples of frequency-dependent template shape at three frequencies. Note that when later used to create profiles, the template amplitudes from different frequencies were modulated based on a spectral index of -1.8.
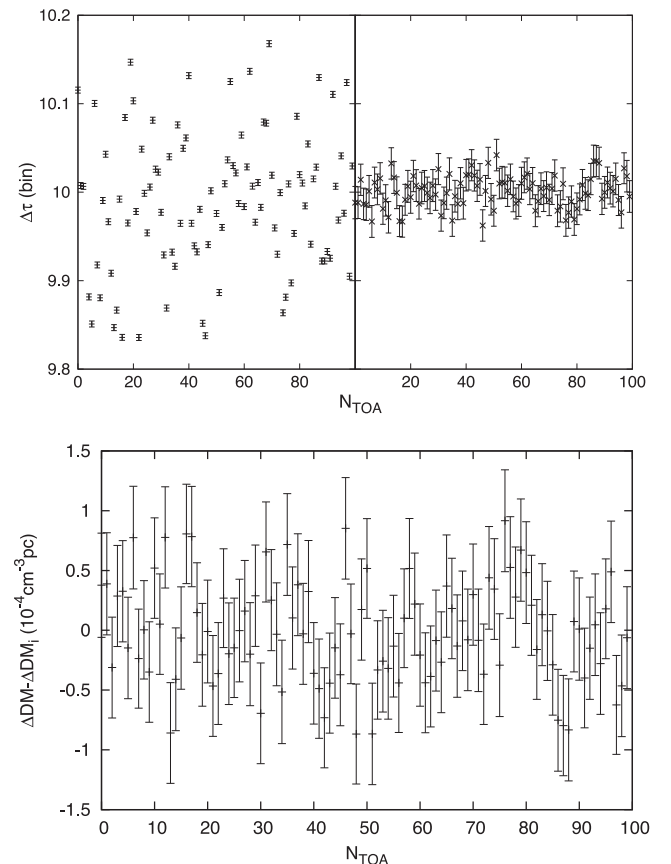

Figure 8. Top: fitted $\Delta\tau$ values of 100 profiles whose DM offsets from the template follow a Gaussian distribution with standard deviation 2×10^{-4} cm^{-3} pc. The assumed observing bandwidth is 500 MHz, from 1.2 to 1.7 GHz. The input phase offset is 10 bins. Here, we used an S/N of 10^3 and kept 16 frequency bands when fitting for both $\Delta\tau$ and ΔDM. The fit is carried out both without (left-hand panel) and with (right-hand panel) a fit for ΔDM. The measurements including a ΔDM fit have a reduced χ^2 of 1.01, while those without result in a reduced χ^2 of the order of ∼650. Bottom: fitted ΔDM from the top right plot after subtraction of the input DM offset, ΔDM$_i$. The corresponding reduced χ^2 is 1.02.
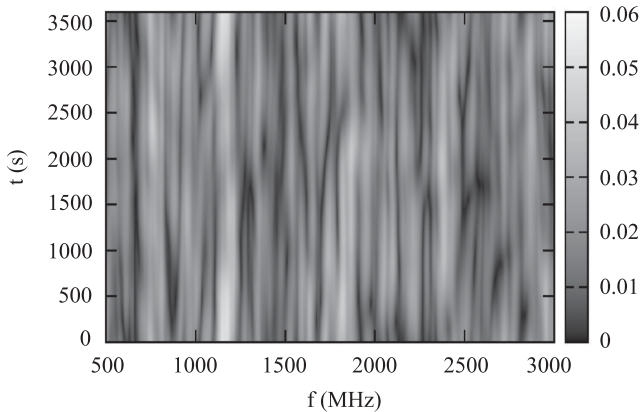
Figure 9. Example simulated dynamic spectrum with length 1 h and frequency coverage from 500 MHz up to 3 GHz. The time and frequency resolution are 10 s and 5 MHz, respectively. The scale is given on the right-hand side.

are scattered beyond the tolerance of the measurement uncertainties if the variable DM values are not accounted for. On the contrary, fitting for both parameters results in $\Delta\tau$ and ΔDM values consistent with the input, and with reduced χ^2 values close to unity for both measurement sets.

3.2.2 Reducing broad-band data

As mentioned in Section 1, the profile shape variability related to diffractive scintillation would be most significant for broad-band pulsar timing data. In order to demonstrate the improvement in timing precision with the channelized DFT method in this case, we simulated data covering a frequency range from 500 MHz up to 3 GHz. In total, we created 1 h observations on 100 epochs. For each epoch, to better simulate real observations, we generated a dynamic spectrum assuming a scintillation time-scale of 20 min and frequency scale of 50 MHz[6], respectively. An example of such a spectrum can be found in Fig. 9. To create data at a given epoch, we first generated profiles for every 10 s and 5 MHz, based on the template shape in Fig. 7. Here we assumed a profile S/N of 20 at 1.4 GHz based on 5 MHz bandwidth and a 1 h integration. Then the amplitudes of the profiles were weighted differently with respect to the dynamic spectrum. Next the profiles were integrated over the whole 1 h session to be used for ToA measurements. When performing the channelized DFT method, we kept a frequency resolution of 50 MHz.

The results are summarized in Fig. 10. It can be seen that using the channelized DFT method in both modes (with and without a ΔDM fit) succeeds in obtaining measurement residuals with reduced χ^2 close to unity. The factor of nearly 2 difference in the measurement precision is due to the correlation between $\Delta\tau$ and ΔDM which still corresponds to a correlation coefficient of approximately 0.65. Simply applying the traditional template-matching approach to the data after averaging over all frequency channels leads to precision more than two orders of magnitude worse and a reduced χ^2 value of approximately 600.

---

[6] Note that when generating the dynamic spectra, we did not consider the dependence of the scintillation time-scale and frequency upon observing frequency. However, the simulation is sufficient for demonstrating the potential improvement from the new algorithm.
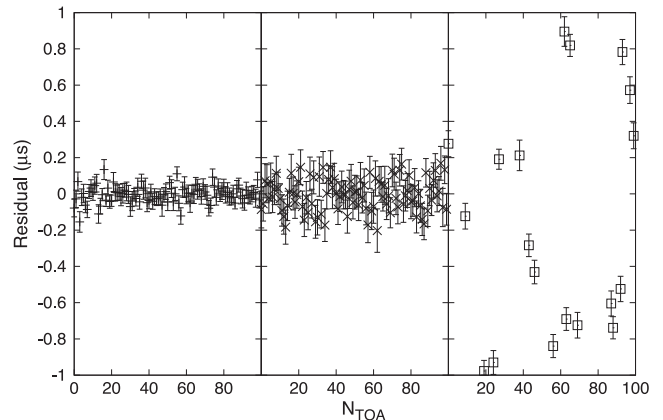

Figure 10. Measurements of $\Delta\tau$ from 100 simulated profiles, which include a shape dependence with observing frequency and flux variation due to diffractive scintillation. Applying the channelized DFT method without a ΔDM fit (left-hand panel) leads to measurement residuals of rms 47 ns and reduced χ^2 of 1.07. Including a simultaneous ΔDM fit (middle panel) reduces the precision to 90 ns while the corresponding measurement reduced χ^2 remains close to unity (0.97). The application of the traditional template-matching approach to the data after averaging over all frequency channels (right-hand panel) results in an rms of 4.3 μs and a reduced χ^2 of approximately 600. Not all of the data points are therefore shown in the plot.

4 APPLICATION TO REAL DATA

4.1 Data

Timing observations of millisecond pulsars have been conducted regularly at the Nançay Radio Telescope. The legacy Berkeley-Orleans-Nançay (BON) backend has been in operation for nearly 10 years, capable of producing 128 MHz data which are coherently dedispersed online (Cognard & Theureau 2006). The Nançay Ultimate Pulsar Processing Instrument (NUPPI), which started in late 2011, is a baseband recording system using a Reconfigurable Open Architecture Computing Hardware field-programmable gate array (FPGA) board developed by the CASPER group[7] and graphics processing units (GPUs). Here the analogue-to-digital converters first sample and digitize the signal over a 512 MHz band at the Nyquist rate with dual polarizations in 8 bits. Then a polyphase filter bank is performed to channelize the band into 128 channels each of 4 MHz width. Next the channels are packetized into four sub-bands and sent to four GPU clusters individually via 10 GbE links for online coherent dedispersion, at a DM of 10.3940 cm^{-3} pc for PSR J1909−3744. Finally, the data were folded to form 1 min integrations.

NUPPI data of PSR J1909−3744 provide a good opportunity to test the application of the channelized DFT approach, as this pulsar is known to show significant flux variation due to interstellar scintillation with frequency scale of the order of ∼50 MHz (e.g. Cordes & Lazio 2002), and thus less than the observing bandwidth. Accordingly, we chose data collected from ∼30 epochs between MJD 56545 and 56592, with central frequency at 1488 MHz. The data were calibrated for polarization with the common single-axis model (e.g. Ord et al. 2004), with reference to a noise diode positioned at 45 deg to the linear feed probes. The PSRZAP and PAZI programs (PSRCHIVE's RFI zapper) were used to clean any RFI. We

---

[7] http://casper.berkeley.edu/

formed a two-dimensional analytic template by fitting Gaussian components to the integration (e.g. Kramer 1994) on MJD 56592 when the source was the brightest among our selected epochs. With the remaining data, we generated integrations of 18–25 min length, with an ephemeris determined from the data produced by the legacy BON backend with a baseline of 8 yr. Most of the preprocessing was conducted with the PSRCHIVE software package (Hotan, van Straten & Manchester 2004).

4.2 Results

The scintillation has been significant within our observing frequency band. In Fig. 11, we divide the whole bandwidth into four 128 MHz sub-bands and show the observed flux densities of the top three divided by that of the bottom one for all epochs. The ratios are seen to vary greatly for different epochs, mostly within the scale of 10^{-2}–10.

For comparison, we applied both the traditional template-matching approach and the channelized DFT method to measure the ToAs of the PSR J1909−3744 integrations. Then, we used the TEMPO2 software package (Hobbs, Edwards & Manchester 2006) to calculate the timing residuals based on the aforementioned ephemeris, without fitting for any parameters. When generating ToAs with the traditional method, we dedispersed the data with DM values both retained from online coherent dedispersion and determined by fitting for a constant DM with multifrequency ToAs from the same data set.

A brief summary of the timing results can be found in Table 1. It can been seen that application of the channelized DFT method (without fitting for ΔDM) achieves the lowest weighted timing precision and improves the ToA measurement uncertainties by ~20 per cent in median. Using the DM measured from the data set itself (10.3916 cm^{-3} pc) leads to a similar timing precision, while retaining the DM used for coherent dedispersion (10.3940 cm^{-3} pc) results in significantly worse rms and more systematics. This can be explained by the fact that a deviation of DM from the true value may induce additional profile variation across the observing band and enhance the scintillation effect. For demonstration, in Fig. 12 we plot the phase offsets of the observed profile on MJD 56592 at different frequencies, given the DM values as in Table 1. Clearly, the DM value corresponding to lower timing rms gives signifi-
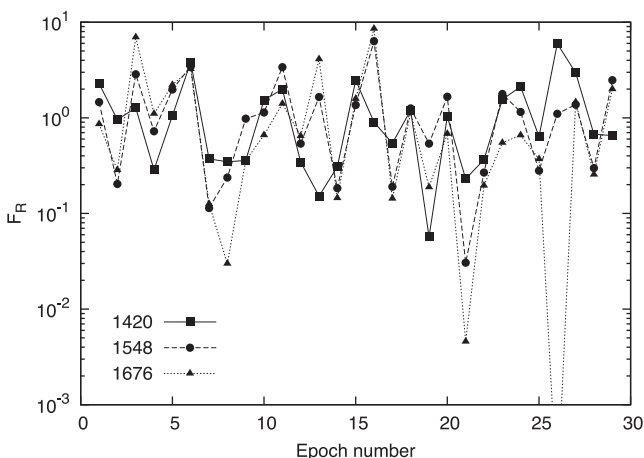
Table 1. Statistical results of ToAs obtained by the traditional template-matching approach (1D) with different DM values for dedispersion and the channelized DFT method without (2D$_0$) and with ΔDM fit (2D$_1$). The DM of 10.3916 cm^{-3} pc was achieved by fitting for a constant DM with multifrequency ToAs from the selected NUPPI data set.

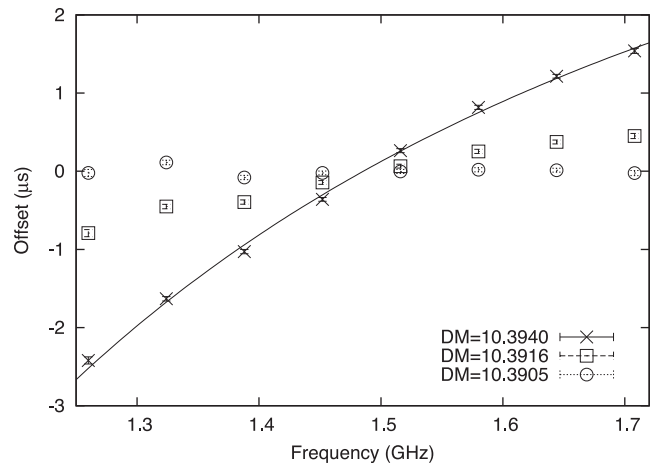| MJD	1D$_0$	1D$_1$	2D$_0$	2D$_1$
DM (cm^{-3} pc)	10.3940	10.3916	10.3940	10.3940
Max. σ_{ToA} (ns)	934	912	839	4094
Min. σ_{ToA} (ns)	39	39	30	220
Median σ_{ToA} (ns)	149	149	114	1014
Weighted rms (ns)	610	275	247	786
Reduced χ^2	40.3	8.13	10.8	1.85

Figure 12. Phase offsets of the observed profile on MJD 56592 at different frequencies based on the DM values as in Table 1. The solid line represents the best-fitting quadratic curve when using DM = 10.3940 cm^{-3} pc. The value of 10.3905 cm^{-3} pc is the best-estimated DM with the offsets.

cantly less differential phase and thus profile variation between frequencies. It is also interesting to notice that after subtracting all quadratic components the offsets are mostly around zero. This indicates that the intrinsic profile variation may not be significant within our observing bandwidth, unless it actually appears as a quadratic drift against frequency.

Applying the channelized DFT method with ΔDM fit results in worse rms residuals, which is expected due to the high correlation between ΔDM and $\Delta\tau$ in the data as indicated in Fig. 1. Nevertheless, in this case including ΔDM into the template-matching fit may not be necessary as DM variations are not significant within the observing time. In Fig. 13, we plot the ΔDM measurements at each epoch, achieved by both the channelized DFT method and ToAs from multiple frequencies as in e.g. Keith et al. (2013). Here, we divided the whole bandwidth into eight 64 MHz sub-bands to create multifrequency ToAs. It can be seen that the two methods lead to consistent measurements, both in values and uncertainties. Within the observing time, there is also no evidence of gradual DM variations above the detection threshold.

5 CONCLUSION

In this paper, we have described the channelized DFT method that can conduct ToA measurements based on timing data with frequency information. The functionality of the channelized DFT method has been tested, and the potential for improvements to
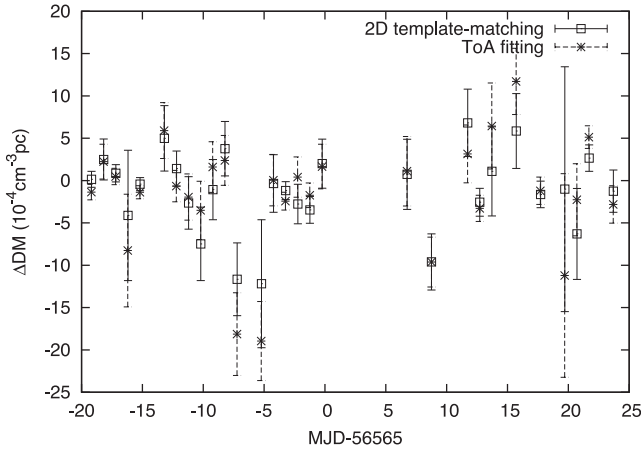

Figure 11. Relative observed flux densities of the top three 128 MHz sub-bands (centred at 1420, 1548, and 1676 MHz, respectively) with respect to the bottom one (centred at 1292 MHz) for all epochs.

Figure 13. Measured ΔDM on each epoch with the two-dimensional template-matching technique and the normal method using multifrequency ToAs. The measurements from template-matching have rms and uncertainty median of 4.8×10^{-4} cm^{-3} pc and 3.2×10^{-4} cm^{-3} pc, respectively, while those obtained based on multifrequency ToAs achieve 6.6×10^{-4} cm^{-3} pc and 2.9×10^{-4} cm^{-3} pc.

timing precision has been demonstrated using simulated data. Furthermore, we have applied the method to timing data of PSR J1909−3744 with 512 MHz bandwidth centred at 1.45 GHz, which removes systematics due to scintillation effects enhanced by a faulty DM value and improves ToA measurement uncertainties by ∼20 per cent in median. Our approach has also been shown to achieve measurements of ΔDM on epochs consistent with methods based on multifrequency ToAs (as in e.g. Keith et al. 2013).

It is known that the observed dispersion delay can deviate from the expected $\propto f^{-2}$ law coming from the cold plasma assumption (e.g. Armstrong, Rickett & Spangler 1995; Keith et al. 2013). This phenomenon can potentially be taken into account with the channelized DFT method, by simply including a theoretical model in the merit function, i.e. equation (8), and enabling more parameter fittings. For this purpose, broad-band observations would be highly requested to break the degeneracy between fitted parameters and to achieve enough sensitivity to measure the deviation.

Note that application of the channelized DFT method might not achieve optimal modelling of DM variations as the measurements use information only from a single observing session without any interpolations over epochs like in other work (Kaspi, Taylor & Ryba 1994; Keith et al. 2013; Lee et al. 2014; Lentati et al. 2014). Nevertheless, if the variation time-scale is well above the intervals between observing sessions, the method can potentially be extended to combine data from neighbouring epochs and perform a global fit for a unique offset in DM, so as to increase the accuracy of determination. Besides, when processing broad-band timing data, the current interpolation approaches do not fully use the information that data from different frequencies are from a simultaneous observation. Therefore, it may also be worth attempting to combine these two types of method, to simultaneously obtain timing residuals and DM modelling directly from timing data.

ACKNOWLEDGEMENTS

REFERENCES

Antoniadis J. et al., 2013, Science, 340, 448
Armstrong J. W., Rickett B. J., Spangler S. R., 1995, ApJ, 443, 209
Bhat N. D. R., Cordes J. M., Camilo F., Nice D. J., Lorimer D. R., 2004, ApJ, 605, 759
Cognard I., Theureau G., 2006, in IAU Joint Discussion, 26th meeting of the IAU, Joint Discussion 2, On the Present and Future of Pulsar Astronomy. Prague, Czech Republic, JD02, #36
Cognard I., Theureau G., Guillemot L., Liu K., Lassus A., Desvignes G., 2013, in Cambresy L., Martins F., Nuss E., Palacios A., eds, SF2A-2013: Proc. Annual Meeting of the French Society of Astronomy and Astrophysics, Nanççay Contribution to the Worldwide Pulsar Programs. p. 327
Cordes J. M., Lazio T. J. W., 2002, preprint (astro-ph/0207156)
Cordes J. M., Shannon R. M., 2010, preprint (astro-ph/1107.3086)
Downs G. S., Reichley P. E., 1983, ApJS, 53, 169
Foster R. S., Backer D. C., 1990, ApJ, 361, 300
Freire P. C. C. et al., 2012, MNRAS, 423, 3328
Hellings R. W., Downs G. S., 1983, ApJ, 265, L39
Hobbs G. B., Edwards R. T., Manchester R. N., 2006, MNRAS, 369, 655
Hotan A. W., van Straten W., Manchester R. N., 2004, Proc. Astron. Soc. Aust., 21, 302
Hotan A. W., Bailes M., Ord S. M., 2005, MNRAS, 362, 1267
Kaspi V. M., Taylor J. H., Ryba M., 1994, ApJ, 428, 713
Keith M. J. et al., 2013, MNRAS, 429, 2161
Kramer M., 1994, A&AS, 107, 527
Kramer M., Xilouris K. M., Camilo F., Nice D., Lange C., Backer D. C., Doroshenko O., 1999, ApJ, 520, 324
Lee K. J. et al., 2014, MNRAS, 441, 2831
Lentati L., Alexander P., Hobson M. P., Feroz F., van Haasteren R., Lee K. J., Shannon R. M., 2014, MNRAS, 437, 3004
Liu K., 2012, PhD thesis, Univ. Manchester
Liu K., Verbiest J. P. W., Kramer M., Stappers B. W., van Straten W., Cordes J. M., 2011, MNRAS, 417, 2916
Lorimer D. R., Kramer M., 2005, Handbook of Pulsar Astronomy. Cambridge Univ. Press, Cambridge
Ord S. M., van Straten W., Hotan A. W., Bailes M., 2004, MNRAS, 352, 804
Osłowski S., van Straten W., Hobbs G. B., Bailes M., Demorest P., 2011, MNRAS, 418, 1258
Pennucci T. T., Demorest P. B., Ransom S. M., 2014, ApJ, 790, 93
Press W. H., Teukolsky S. A., Vetterling W. T., Flannery B. P., 1992, Numerical Recipes: The Art of Scientific Computing, 2nd edn. Cambridge Univ. Press, Cambridge
Ransom S. M., Demorest P., Ford J., McCullough R., Ray J., DuPlain R., Brandt P., 2009, in AAS Meeting Abstracts, Vol. 214, p. 605.08
Stappers B. W. et al., 2011, A&AS, 530, A80
Taylor J. H., 1992, Phil. Trans. R. Soc. A, 341, 117
van Straten W., 2006, ApJ, 642, 1004

APPENDIX A: DERIVATIVE CALCULATIONS FOR L–M ROUTINE

The L–M data modelling routine requires the input of a gradient of χ^2 and the curvature matrix. The calculation was done in Press et al. (1992) for a model of real numbers in a one-dimensional array, and here we derive the expressions concerning complex numbers and two dimensions. With the measurement $y_{j,k} = m_{j,k} + n_{j,k}i$, and the

model $y(x_{j,k}, \boldsymbol{a}) = m(x_{j,k}, \boldsymbol{a}) + n(x_{j,k}, \boldsymbol{a})i$, we have

$$\chi^2(\boldsymbol{a}) = \sum_{j,k} \left| \frac{m(x_{j,k}, \boldsymbol{a}) + n(x_{j,k}, \boldsymbol{a})i - m_{j,k} - n_{j,k}i}{\sigma_{j,k}^2} \right|^2$$

$$= \sum_{j,k} \frac{1}{\sigma_{j,k}^2} [m^2(x_{j,k}, \boldsymbol{a}) + m_{j,k}^2 - 2m(x_{j,k}, \boldsymbol{a})m_{j,k}$$

$$+ n^2(x_{j,k}, \boldsymbol{a}) + n_{j,k}^2 - 2n(x_{j,k}, \boldsymbol{a})n_{j,k}], \quad (A1)$$

where $\boldsymbol{a}$ is an array containing the fitted parameters and $i = \sqrt{-1}$. Hence, the gradient of χ^2 is expressed by

$$\frac{\partial \chi^2}{\partial \alpha_p} = \sum_{j,k} \frac{2}{\sigma_{j,k}^2} \left[\left(m(x_{j,k}, \boldsymbol{a}) - m_{j,k} \right) \frac{\partial m(x_{j,k}, \boldsymbol{a})}{\partial \alpha_p} \right.$$

$$\left. + \left(n(x_{j,k}, \boldsymbol{a}) - n_{j,k} \right) \frac{\partial n(x_{j,k}, \boldsymbol{a})}{\partial \alpha_p} \right], \quad (A2)$$

and the second derivative matrix (Hessian matrix) is written as

$$\frac{\partial \chi^2}{\partial \alpha_p \partial \alpha_q} = \sum_{j,k} \frac{2}{\sigma_{j,k}^2} [m(x_{j,k}, \boldsymbol{a}) \frac{\partial m^2(x_{j,k}, \boldsymbol{a})}{\partial \alpha_p \partial \alpha_q}$$

$$+ n(x_{j,k}, \boldsymbol{a}) \frac{\partial n^2(x_{j,k}, \boldsymbol{a})}{\partial \alpha_p \partial \alpha_q}$$

$$+ \frac{\partial m(x_{j,k}, \boldsymbol{a})}{\partial \alpha_p} \frac{\partial m(x_{j,k}, \boldsymbol{a})}{\partial \alpha_q} + \frac{\partial n(x_{j,k}, \boldsymbol{a})}{\partial \alpha_p} \frac{\partial n(x_{j,k}, \boldsymbol{a})}{\partial \alpha_q}$$

$$- m_{j,k} \frac{\partial m^2(x_{j,k}, \boldsymbol{a})}{\partial \alpha_p \partial \alpha_q} - n_{j,k} \frac{\partial n^2(x_{j,k}, \boldsymbol{a})}{\partial \alpha_p \partial \alpha_q}]. \quad (A3)$$

The actual fitting routine uses the curvature matrix defined as $\alpha_{pq} \equiv \frac{1}{2} \frac{\partial \chi^2}{\partial \alpha_p \partial \alpha_q}$. After eliminating the second derivative terms so as to stabilize the iterations (explained in Chapter 15.5, Press et al. 1992), we then have

$$\alpha_{pq} = \sum_{j,k} \frac{1}{\sigma_{j,k}^2} \left[\frac{\partial m(x_{j,k}, \boldsymbol{a})}{\partial \alpha_p} \frac{\partial m(x_{j,k}, \boldsymbol{a})}{\partial \alpha_q} \right.$$

$$\left. + \frac{\partial n(x_{j,k}, \boldsymbol{a})}{\partial \alpha_p} \frac{\partial n(x_{j,k}, \boldsymbol{a})}{\partial \alpha_q} \right]. \quad (A4)$$

Note that in our model

$$\boldsymbol{a} = (b_1, \ldots, b_{N_b}, \Delta\tau, \Delta\mathrm{DM}), \quad (A5)$$

$$m_{j,k} = P_{j,k} \cos\theta_{j,k}, \quad (A6)$$

$$n_{j,k} = P_{j,k} \sin\theta_{j,k}, \quad (A7)$$

$$m(x_{j,k}, \boldsymbol{a}) = b_j S_{j,k} \cos(\phi_{j,k} + \tau_j), \quad (A8)$$

$$n(x_{j,k}, \boldsymbol{a}) = b_j S_{j,k} \sin(\phi_{j,k} + \tau_j), \quad (A9)$$

then χ^2 becomes

$$\chi^2 = \sum_{j,k} \frac{P_{j,k}^2 + b_j^2 S_{j,k}^2 - 2b_j P_{j,k} S_{j,k} \cos\left(\phi_{j,k} - \theta_{j,k} + k\tau_j\right)}{\sigma_{j,k}^2},$$

$$(A10)$$

and the gradient of χ^2 is written as

$$\frac{\partial \chi^2}{\partial \alpha_p} =$$

$$\begin{cases} \displaystyle\sum_{i} \frac{2b_p S_{p,k}^2 - 2P_{p,k} S_{p,k} \cos(\phi_{p,k} - \theta_{p,k} + k\tau_p)}{\sigma_{p,k}^2}, & 1 \le p \le N_b \\[12pt] \displaystyle\sum_{j,k} \frac{2k b_j P_{j,k} S_{j,k} \sin(\phi_{j,k} - \theta_{j,k} + k\tau_j)}{\sigma_{j,k}^2}, & p = N_b + 1 \\[12pt] \displaystyle\sum_{j,k} \frac{2k D_0 b_j P_{j,k} S_{j,k} \sin(\phi_{j,k} - \theta_{j,k} + k\tau_j)}{\sigma_{j,k}^2 f_j^2}, & p = N_b + 2 \end{cases}$$

$$(A11)$$

and the curvature matrix is

$$\alpha_{pq} = \begin{cases} \displaystyle\sum_{k} \frac{S_{p,k}^2}{\sigma_l^2}, & 1 \le p, q \le N_b, p = q \\[10pt] 0, & 1 \le p, q \le N_b, p \ne q \\[6pt] 0, & 1 \le p \le N_b, N_b \le q \le N_b + 2 \\[10pt] \displaystyle\sum_{j,k} \frac{k^2 b_j^2 S_{j,k}^2}{\sigma_j^2}, & p = q = N_b + 1 \\[10pt] \displaystyle\sum_{j,k} \frac{k^2 D_0 b_j^2 S_{j,k}^2}{\sigma_j^2 f_j^2}, & p = N_b + 1, q = N_b + 2 \\[10pt] \displaystyle\sum_{j,k} \left(\frac{k D_0 b_j S_{j,k}}{\sigma_j f_j} \right)^2, & p = q = N_b + 2. \end{cases}$$

$$(A12)$$

This paper has been typeset from a TeX/LaTeX file prepared by the author.